Supporting Information

A Co-containing polyoxogemanotungstate for alkaline electrocatalytic water oxidation

Da-Huan Li,† Lei Jia,† Yi-Xin Liu, Cai Sun, Xin-Xiong Li, Ping-Wei Cai, Yan-Qiong Sun* and Shou-Tian Zheng*

College of Chemistry, Fuzhou University, Fuzhou, Fujian 350108, China.

*Email: sunyq@fzu.edu.cn; stzheng@fzu.edu.cn

Contents

1. Materials and Methods

Chemicals and materials:

Cobaltous chloride [$CoCl_2 \cdot 6H_2O$, ≥99.0%], boric acid [SeO_2, ≥99.0%], tungsten trioxide [WO_3, ≥99.0%], sodium carbonate [Na_2CO_3, ≥99.8%], acetylene black (AB), 5 wt% of Nafion solution, isopropyl alcohol [C_3H_8O, ≥99.0%] and Commercial Cobalt Tetraoxide [Co_3O_4, ≥99.0%] are all analytical grades purchased from Sinopharm Chemical Reagent Co. Ltd. Which were all used without any extra purification.

Synthesis of Co_9-POT:

The synthesis of $K_8Na_2[A\text{-}\alpha\text{-}GeW_9O_{34}] \cdot 25H_2O$ (GeW_9) was performed based on the reported literature.[1] 0.305 g $K_8Na_2[A\text{-}\alpha\text{-}GeW_9O_{34}] \cdot 25H_2O$, 0.051 g $CoCl_2 \cdot 6H_2O$, 0.051 g SeO_2, 0.103 g Na_2CO_3, and 8 mL deionized water were added to a 20 mL vial to form a suspension. The mixture was stirred for 1 h, and then heated at 65 ºC for 72 h. After being cooled slowly to room temperature, the purple block crystals **Co_9-POT** were obtained by further washing with distilled water and drying completely.

Characterization:

High-resolution TEM (HRTEM) together with its element mapping was carried out on the TEM (FEI Talos F200S G2) to further understand the microstructure details. X-ray photoelectron spectroscopy was used to analyze the samples' surface composition (XPS, ESCALAB 250). Powder X-ray diffraction (PXRD) patterns were obtained on a Rigaku Ultima IV diffractometer, X'PertPRO with Cu-Kα radiation (λ = 1.54056 Å), and MiniFlex II. Thermogravimetric (TG) analysis was carried out on a Mettler Toledo Star TGA/DSC1 analyzer under nitrogen atmosphere at a ramp rate of 10 ºC /min. The instrument of Quadrasorb SI (Quantachrome) was performed for the N_2 sorption/desorption analysis. Infrared (IR) spectra (KBr particles) were obtained using a Nicolet IS 50 FT-IR spectrometer in the range of 400-4000 cm^{-1}. Inductively coupled plasma optical emission spectrometry (ICP-MS) was carried out by using a SHIMADZU ICPE-9820 instrument. Single-crystal X-ray diffraction data for **Co_9-POT** was collected on a XtaLAB Synergy with Mo K_α radiation (λ = 0.71073 Å) at 293 K equipped with a graphite monochromator. The crystal structure was solved by the direct method and refined by the full-matrix least-squares method on F^2, using SHELXL and Olex2.[2, 3] All non-hydrogen atoms were refined anisotropically. The contribution

of these disordered solvent molecules to the overall intensity data of all structures was treated using the SQUEEZE method in PLATON.[4] Crystallographic data for the structures reported have been deposited in the Cambridge Crystallographic Data Centre with CCDC reference numbers 2362096 for the compound. These data can be obtained free of charge from the Cambridge Crystallographic Data Centre at www.ccdc.cam.ac.uk/data request/cif. The selected crystal parameters, data collection, and refinements are summarized in Table S1†.

Electrochemical characterization:

The preparation of the working electrode. First, 0.1 g of acetylene black (AB) was treated in 3 M HNO_3 for 12 h at room temperature with stirring, then washed with deionized water and dried by centrifugation before being prepared for use. The treated AB surface had more defects. For the preparation of the working electrode, 3 mg of catalyst and 2 mg of conductive AB were dispersed in a mixed solution containing 120 μL of isopropyl alcohol and 370 μL of 5 vol% aqueous Nafion. The AB was added to improve the conductivity of the electrode. The addition of conductive carbon can greatly improve the catalytic activity of metal oxide catalysts, and the contribution of carbon to the OER current is negligible in the potential range studied (Fig. S10†). Then, the suspension was ultrasonicated for 30 minutes to form a homogeneous ink. The carbon cloth (CC) was first degreased by sonication in acetone and carefully washed with 0.5 M HCl in an ultrasonic bath for 20 min to remove the surface oxidation layer. Finally, apply 50 μL of catalyst ink in a uniform drop onto a CC with an area of 1 × 1 cm^2 and controlled catalyst loading of 0.5 mg cm^{-2}. For comparison, we prepared three working electrodes **Co_9-POT**, Co_3O_4 and WO_3 under the same conditions.

Electrochemical OER Measurements. The OER electrochemical measurements were performed on the Zennium-pro electrochemical workstation (ZAHNER elektrik, Germany) using a standard three electrode system. The catalyst films on CC were used as the working electrode and carbon rod electrode was used as the counter electrode, a saturated calomel electrode (Hg/HgO, filled with 0.1 M KOH) as the reference electrode. The test electrolyte is 0.1 M aqueous KOH solution (pH = 13) and normalized concerning the reversible hydrogen electrode (RHE) according to Equation: $E_{vs\cdot RHE} = E_{vs.Hg/HgO} + 0.0591 \times pH + E^0_{Hg/HgO}$ ($E^0_{Hg/HgO} = 0.098$ V). All potentials have been converted to RHE without specific indication. Before electrochemical data collection, electrode were activated by cyclic voltammogram (CV) measurements performed at a scan rate of 50 mV s^{-1} until a constant curve was obtained. The OER polarization curves were obtained using linear scanning voltammetry at a scan rate of 5 mV s^{-1}, and correction of the stable current issue by 91% *iR* compensation. The Tafel slopes were calculated from the linear region of the LSV polarization curve according to the equation: $\eta = b \times \log j + a$, in which η is the overpotential, b is the Tafel slope, and j is the current density. To evaluate the charge transfer resistance, the EIS was performed at open circuit potential with an AC voltage amplitude of 5 mV and a frequency of 0.1 Hz to 100 KHz, the charge transfer resistance (R_{ct}) was calculated from the diameter of the semicircle in the Nyquist plots. The specific activities were obtained by normalizing the current density for electrochemically active surface areas (ECSAs). ECSA were acquired according to the equation: ECSA = $R_f \times S$, where R_f is the roughness factor and S is the geometric area of the working electrode. In this study, S = 1 cm^{-2}. The double-layer capacitance (C_{dl}) based on the smooth oxide surface ($C_S \sim 40$ μF cm^{-2}) was determined using $R_f = C_{dl} / C_S$ to determine R_f.[5] The electrochemical C_{dl} was estimated by CV scans in a non-Faradic region at various scan rates from 20 to 120 mV s^{-1}. Specifically, the value of C_{dl} was fitted by plotting $\Delta j = (j_a - j_c)$ at 0.975V against the scan rate, whereby, j_a and j_c are the anode and cathode current densities, respectively. Assuming that the current is due to double layer charging, the slope of the fitted line was the twice of C_{dl}. The turnover frequency (TOF) were calculated from the activity of the catalysts per active site following the equation: TOF = $j \times A_{geo} / (n \times F \times m_{site})$, where j is the current density at a potential, A_{geo} is the electrode area, n is the number of electrons (4 for OER), F is the Faraday constant (96485 C/mol), and m_{site} is the total number of metal sites.[6] The TOFs were calculated assuming that all the metal Co atoms were catalytically active, therefore representing the lower limit of the activity. In the end, the stability measurement for OER was tested by the

chronoamperometry method for 20 h at 10 mA cm^{-2}. All experiments were performed at room temperature.

Faraday efficiency (FE) testing of Co_3O_4 and **Co_9-POT** using the rotating ring-disk electrodes (RRDE) technique in N_2-saturated 0.1 M KOH solution. Before detecting O_2 species, high-purity N_2 gas was bubbled through the solution for at least 30 min to remove the dissolved O_2. The FE was obtained according to the previous literature:[7, 8]

$$FE = \frac{I_{ring}}{C_e \times I_{disk}}$$

Here, I_{disk} is the current at a constant potential (1.5 $V_{vs\ RHE}$) on the disk electrode, I_{ring} is the collection current on the Pt ring electrode at a constant potential of 0.4 $V_{vs\ RHE}$, C_e is the oxygen collection coefficient (~0.2) for this type of electrode configuration.

In Situ Raman Spectra Measurements. Raman spectra were detected by an Invia type micro confocal Raman spectrometer (Renishaw, UK). A 473 nm excitation laser beam (6 mW) with a spot size of 1-2 μm was selected, and the spectral offset was routinely calibrated using a silicon wafer (520.7 cm^{-1}). Spectral acquisition time was 5-30 s. In situ Raman spectra were measured in 0.1 M KOH using a three-electrode cell consisting of a 4 mm gold disk working electrode, a Hg/HgO reference electrode, and a platinum wire counter electrode. Other conditions were the same as for the electrochemical measurements described above. Relative to the RHE, the applied anodic potentials ranged from 1.1 V to 1.5 V, at intervals of 0.05 V. A five-minute timer test was performed on the OER catalysts prior to the chronoamperometric of Raman spectra at each potential.

2. Additional Tables

Table S1 Crystal data and structure refinement parameters for **Co_9-POT.**

Compound	**Co_9-POT**
Empirical formula	$H_{200}Co_{18}Ge_6K_{18}Na_6O_{312}Se_4W_{54}$
Crystal system	Trigonal
Space group	$R\bar{3}$
a (Å)	32.3512(3)
b (Å)	32.3512(3)
c (Å)	25.9508(4)
α (°)	90
β (°)	90
γ (°)	120
V (Å^3)	23521.3(6)
Z	3
F (000)	22782
crystal size	0.40mm × 0.35mm × 0.25mm
ρ_{calcd} (g cm^{-3})	3.671
Temperature (K)	293(2)
μ (mm^{-1})	22.021
Refl. Collected	54552
Independent relf	9249
GOOF	1.082
R_1 [I >2σ]	R_1^a = 0.0466, wR_2^b = 0.1099
R_1 (all data)	R_1^a = 0.0508, wR_2^b = 0.1118

$^{[a]}R_1 = \sum||F_o|-|F_c||/\sum|F_o|$, $^{[b]}wR_2 = \{\sum[w(F_o^2-F_c^2)^2]/\sum[w(F_o^2)^2]\}1^{1/2}$

Table S2. Bond values and calculations for each atom in **Co_9-POT.**

Atoms code	Bond Valence	Valence state
W1	6.11100	6
W2	6.06642	6
W3	6.02259	6
W4	6.32547	6
W5	6.00521	6
W6	5.62985	6
W7	6.22573	6
W8	6.05246	6
W9	6.28603	6
Co1	2.01921	2
Co2	2.05761	2
Co3	1.96811	2
Ge1	3.95408	4
Se1	4.08291	4
Se2	4.23077	4

Table S3. Comparison of OER performance of **Co_9-POT** and POM-based electrocatalysts

samples	Electrolyte	Overpotential (mV)@10 $mA \cdot cm^{-2}$	Ref.
Co_9-POT	0.1 M KOH	341	this work
$Co_4(PW_9)_2$@Co/Ni@C	0.1 M KOH	400	[9]
$Co_4(PW_9)_2$@N, S-Co@C	0.1 M KOH	410	[9]
$Co_4(PW_9)_2$@Co@C	0.1 M KOH	430	[9]
Co_3O_4	0.1 M KOH	439	this work
$Co_4(PW_9)_2$@N,S-Co/Ni@C	0.1 M KOH	460	[9]
SiW_9Co_3@ZIF-67	0.1 M KOH	470	[10]
WO_3	0.1 M KOH	610	this work
AB&PS-13 ($AlMo_6$)	1 M KOH	330	[11]
{$Cu_2SiW_{12}O_{40}$}@HKUST-1	1 M KOH	340	[12]
$(C_5H_7N_2)_6[NiW_{12}O_{44}]$	1 M KOH	347	[13]
$[Ni_2(BBTZ)(H_2O)_4]V_4O_{12}\cdot 2H_2O$	1 M KOH	353	[14]
PW_6Mo_6/ZIF-67@NF	1 M KOH	370	[15]
PW_{12}/Ag/graphene-a	0.1 M PBS	540	[16]
GeW_9@NiF	PBS (pH=7)	530	[17]

Table S4. Fitted data of the electrochemical impedance spectroscopy analysis.

samples	R_0/Ω	CPE_1/mF	R_1/Ω	CPE_2/μF	R_2/Ω	Overall Error
WO_3	2.27	0.96	1580	151	31.2	3.39%
Co_3O_4	2.23	0.745	81.5	134	22.6	2.63%
Co_9-POT	2.11	2.16	42.4	188	1.43	1.98%

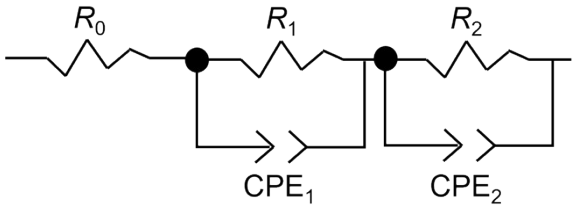

The equivalent circuit is used in fitting the plot.

R_0: solution resistance; R_1 or R_2: charge transfer resistance; CPE_1 or CPE_2: constant phase element. The two *R*-CPE units represent two electransfer processes. One is the electrochemical oxidation of H_2O by electron transfer at the liquid-solid interface. The other is the transfer of electrons to a carbon cloth electrode via a catalyst. The former was a more sluggish process than the latter.[18, 19] Therefore, a larger charge transfer resistance (R_1) corresponds to the electrochemical charge transfer process.

Table S5. Inductively coupled plasma spectroscopy (ICP) analysis for Co_3O_4.

Samples	$C_{e/Co}$ (mg/L)	Co_3O_4 (%)
Co_3O_4 (CV)	0.69	9.41
Co_3O_4 (20-h it)	2.84	38.68

Table S6. The characteristic time constant (τ, s) of **Co_9-POT**.

E_{RHE}/V	C_{dl}/mF cm^{-2}	R/Ω	Phase angle/θ	τ/s
1.0	4.70	3521	78.7	16.53
1.1	4.61	3756	79.6	17.33
1.2	4.75	3562	76.5	16.93
1.3	4.76	3316	71.1	15.79
1.4	4.94	2421	70.5	11.97
1.5	4.52	937	64.2	4.24
1.6	4.53	58	55.1	0.263
1.7	4.44	14	32.9	0.062

EIS measurements were carried out to determine the ECSA of the prepared catalyst films and to investigate the electrochemical properties of the catalysts in relation to the applied potential. The CPE has two degrees of freedom; (i) the coefficient, Q, related to the electrode capacitance, and (ii) the constant phase exponent, α. For $\alpha = 1$, the EIS response is that of an ideal parallel capacitor. For $0 < \alpha < 1$, the behavior of the double-layer capacitance deviates from ideality dependent on the surface roughness and dispersion of the frequency. Based on an equation of Brug et. al.[20] the double-layer capacitance can be estimated:

$$C_{dl} = \left[Q \times \left(\frac{1}{R_0} + \frac{1}{R_{ct}} \right)^{(a-1)} \right]^{\frac{1}{a}}$$

where C_{dl} is the interfacial capacitance,

Q the CPE coefficient,

α the constant phase component ($\alpha \sim 0.88$),[21]

R_0 the electrolyte resistance,

R_{ct} the charge transfer resistance (R_1).

The characteristic time constant (τ, s) of the charge transfer process is the product of the charge transfer resistance (R, Ω) and the double-layer capacitance (C_{dl}, F), i.e. $\tau = R \times C_{dl}$. As the applied potential was increased, the value of C_{dl} also increased up to an apparent maximum. Interestingly, the increase in the capacitance coincided with the onset of significant oxygen volution current. Therefore, this variation in the value of C_{dl} is likely a reflexion of the increasing concentration of charged surface states as the OER progresses.

3. Additional Figures

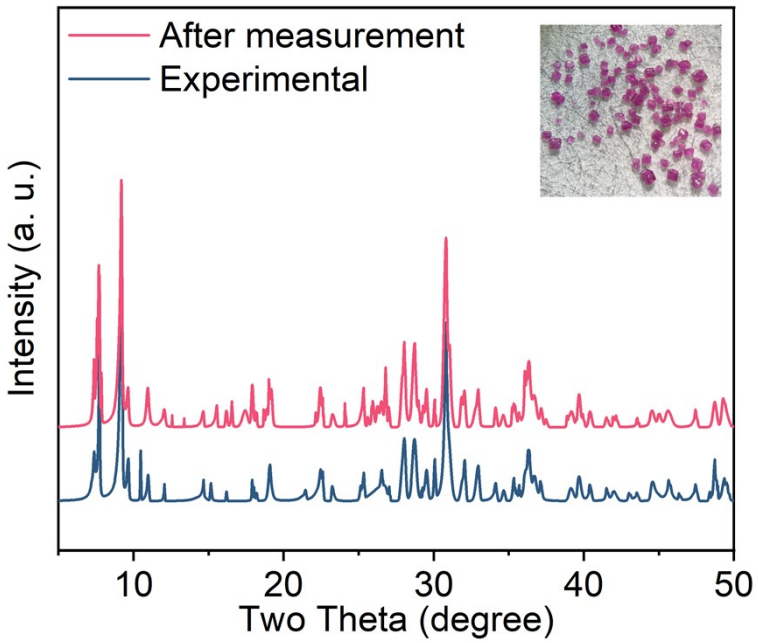

Fig. S1 Simulated and experimental PXRD patterns of **Co_9-POT** (inset: Crystal photo).

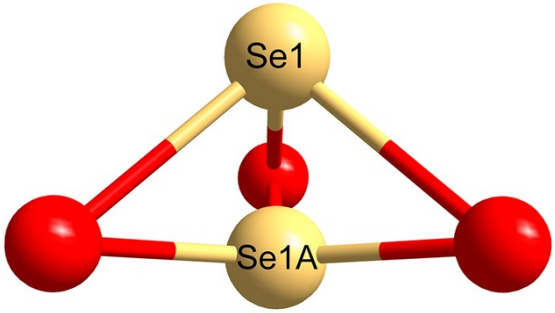

Fig. S2 The Se1 atom is split into two sites: Se1 and Se1A. Atomic color code: Se, pale yellow; O, red.

Fig. S3 The structure of {Co_3} cluster. Atomic color code: Co, pink; O, red.

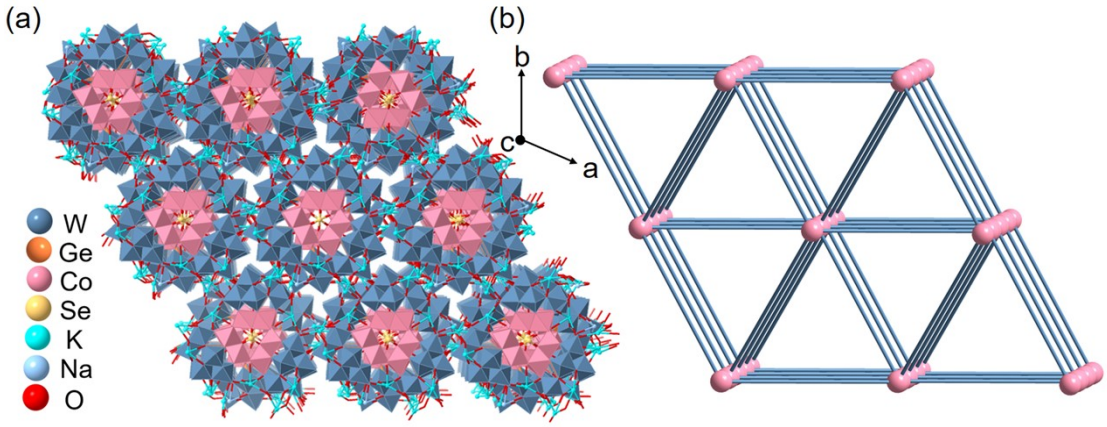

Fig. S4 (a) View of the three-dimensional inorganic framework structure of **Co_9-POT** along the *c*-axis. (b) Topological representation of a four-connected *dia*-type net for **Co_9-POT**, in which pink atoms represent $\{Co_9Se_2(Ge_3W_9)_3\}$ clusters and pale blue bonds represent K^+ ions.

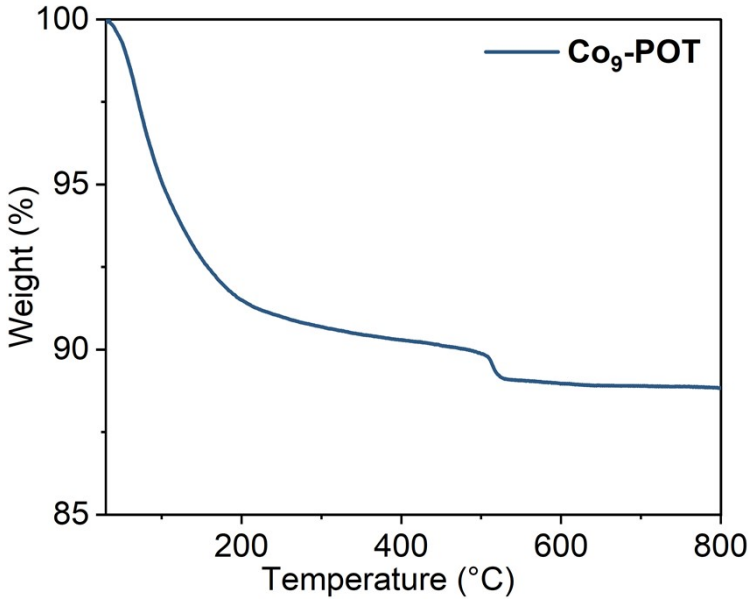

Fig. S5 The TG curve of **Co_9-POT**.

The thermal stability of **Co_9-POT** is determined by thermogravimetric analysis at a heating rate of 10 ºC/min in an argon atmosphere from 30 ºC to 800 ºC. As shown in Fig. S5†, **Co_9-POT** has a continuous weight loss process in the temperature range of 30 ºC to 800 ºC. The initial weight loss of 8% from 30 ºC to 200 ºC corresponds to approximately 39 lattice water molecules per formula. After 200 ºC, **Co_9-POT** begins to decompose and converts to oxide.

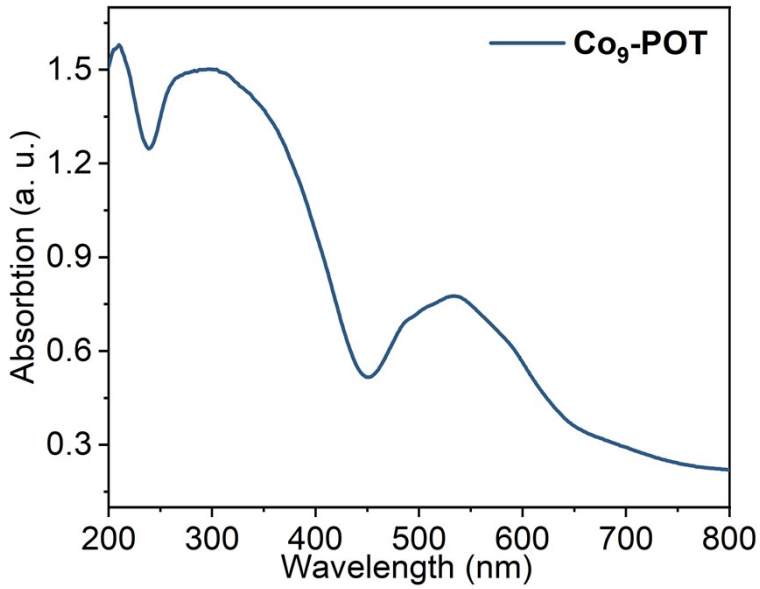

Fig. S6 Solid UV diffuse reflection spectrum of **Co_9-POT**.

The UV diffuse spectrum of **Co_9-POT** is determined in the range of 200 to 800 nm. The absorption peak in the range of 200 to 220 nm can be attributed to the charge transfer transitions from O to W. The absorption peak in the 260 nm and 535 nm correspond to the charge transfer between O to W and the d-d charge transfer between Co^{2+}, respectively.[22]

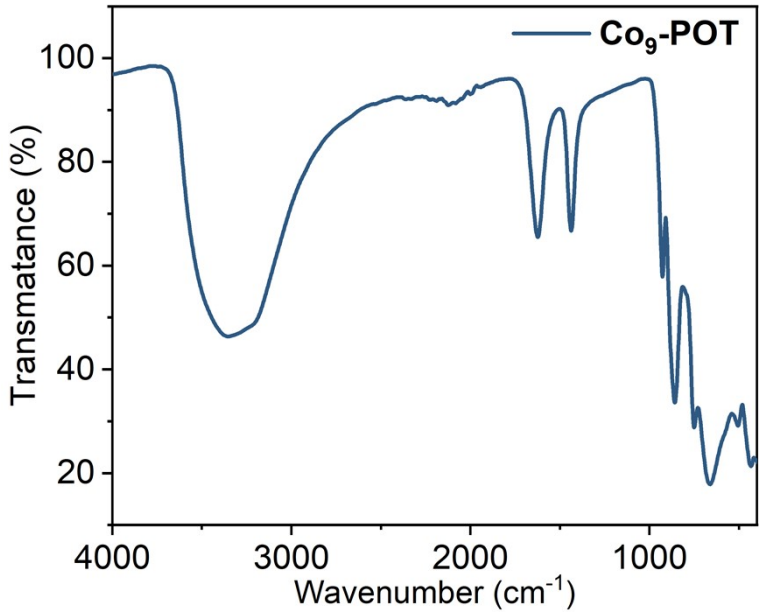

Fig. S7 IR spectra of **Co_9-POT**.

The FT-IR spectra were measured in the range of 400-4000cm^{-1} with KBr pallets. The strong peaks around 3400 and 1630 cm^{-1} are dominated by the stretching and bending modes of the water molecules. The characteristic bands derived from the Keggin POM fragments in the 721-1030cm^{-1} region. In detail, the peak at 1040 and 938cm^{-1} for **Co_9-POT** is attributed to ν(Ge-O) and (Ge-O_t). The peak at 806, 721, and 692cm^{-1} is attributed to ν(M-O-M) (M = Co or W).[23, 24]

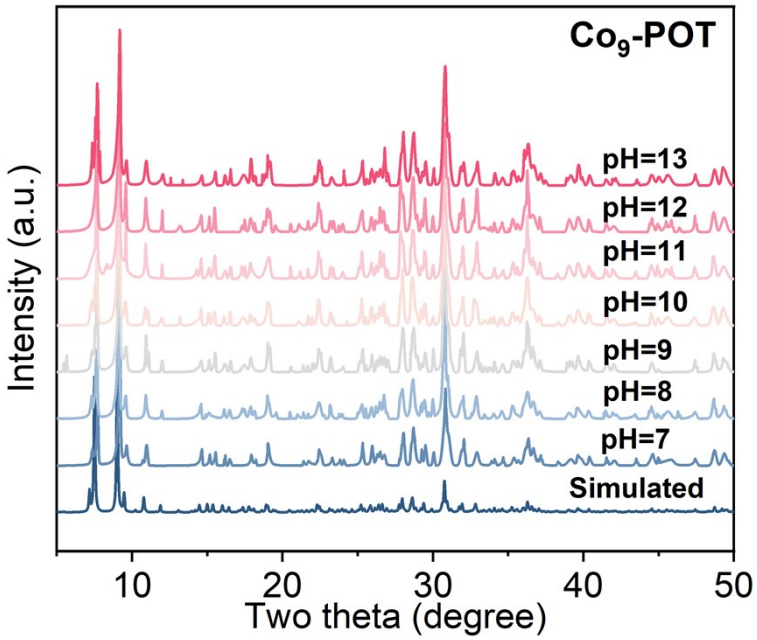

Fig. S8 The pH stability of **Co_9-POT** in the range of 7 to 13.

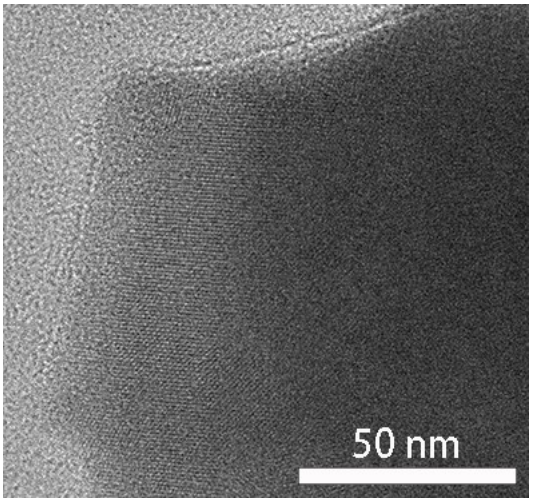

Fig. S9 TEM images of **Co_9-POT** at local magnification.

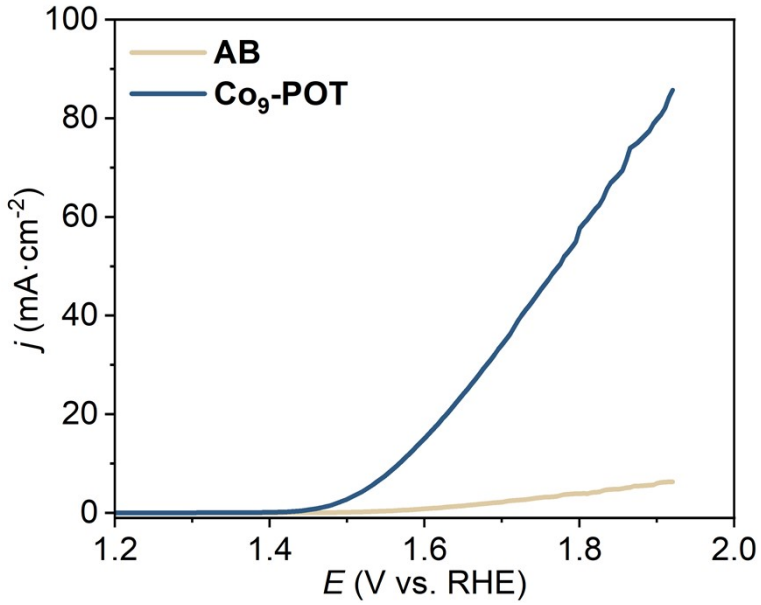

Fig. S10 Electrochemical activity diagram with LSV curves of bare AB and **Co_9-POT**.

For the metal oxide-based catalysts, the total mass loading is 0.5 mg cm^{-2}, including the metal oxide of 0.3 mg cm^{-2} and the carbon additive of 0.2 mg cm^{-2}. For pure carbon material, the mass loading is also 0.5 mg cm^{-2} for a fair comparison. Given the low conductivity of oxides, carbon materials were commonly added as simple conductive additives to provide good electrical conductivity, which was widely adopted by plenty of previous studies.[25] We emphasize that the current contribution from our AB is very small and can be negligible. For example, at 1.60 V versus RHE, the current density for the Bare AB is a mere ~ 0.81 mA cm^{-2}, greatly smaller than that of 15.6 mA cm^{-2} for the **Co_9-POT** catalyst.

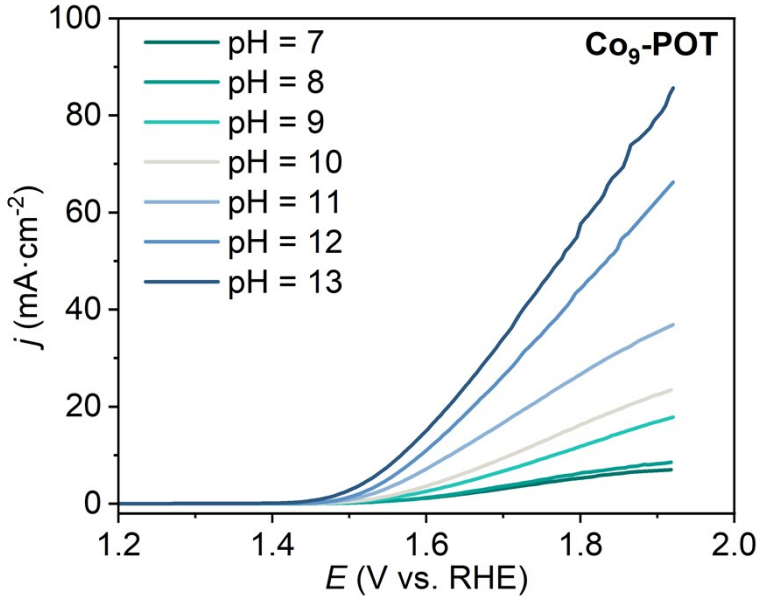

Fig. S11 Comparison of LSV activities of **Co_9-POT** in different pH electrolytes.

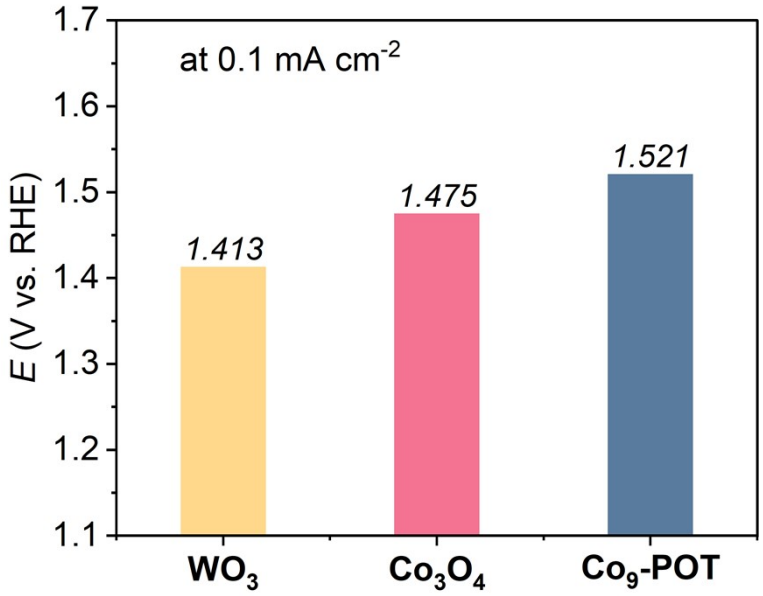

Fig. S12 The onset potentials of Bara AB and **Co₉-POT**. The onset potential (E_{onset}) is defined as the potential required to reach an OER current density of 0.1 mA cm^{-2}.

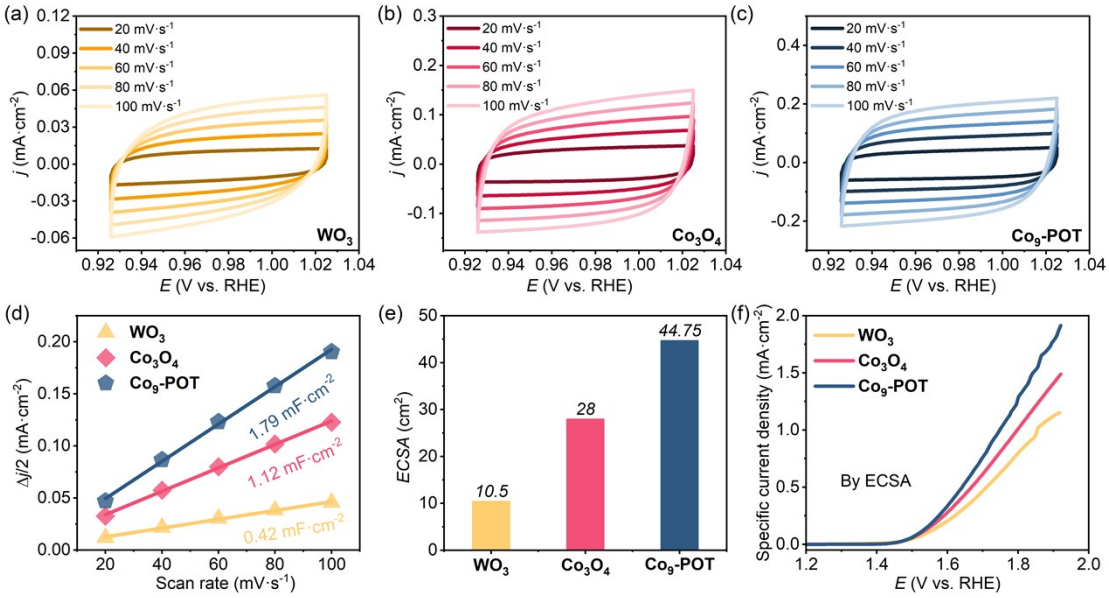

Fig. S13 CV curves for OER in 0.1 M KOH solution at a scan rate of 20, 40, 60, 80, and 100 and mV s^{-1}: (a) WO_3, (b) Co_3O_4, (c) **Co₉-POT**; (d) Capacitive current density as a function of scan rates of different catalysts, with the double layer capacitance values listed; (e) ECSA of each sample; (f) The normalized OER current density according to their ECSAs.

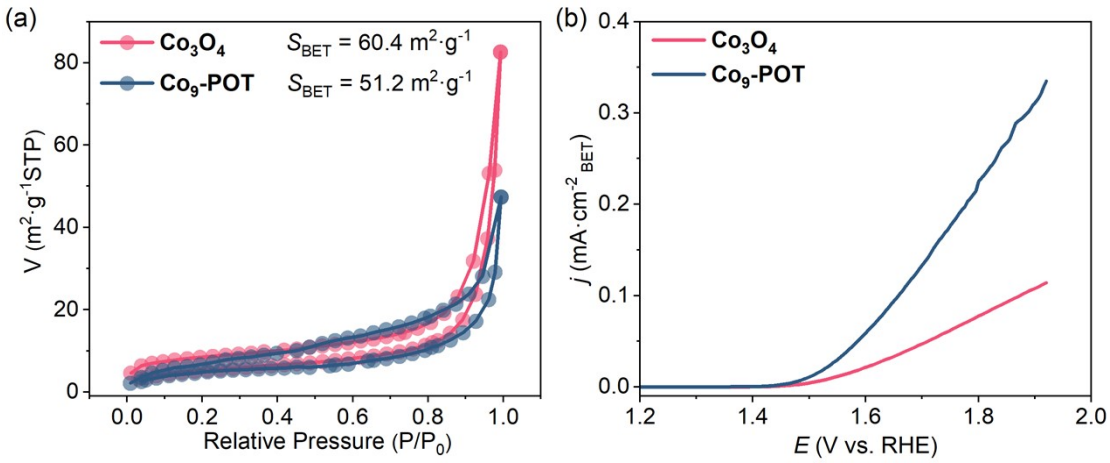

Fig. S14. (a) N_2 adsorption-desorption isotherms of **Co_9-POT** and Co_3O_4; (b) LSV curves after BET-normalized.

In order to facilitate a more accurate comparison of the actual catalytic activities of **Co_9-POT** and Co_3O_4, the N_2 adsorption-desorption isotherms of the **Co_9-POT** and Co_3O_4 were initially tested. The specific surface area of **Co_9-POT** was calculated to be 51.2 m^2 g^{-1}, which was lower than that of Co_3O_4, which exhibited a value of 60.4 m^2 g^{-1} (Fig. S14a). The LSV curve was plotted using the normalized specific surface area as shown in Fig. S14b. It can be observed that **Co_9-POT** still has higher electrocatalytic OER activity.

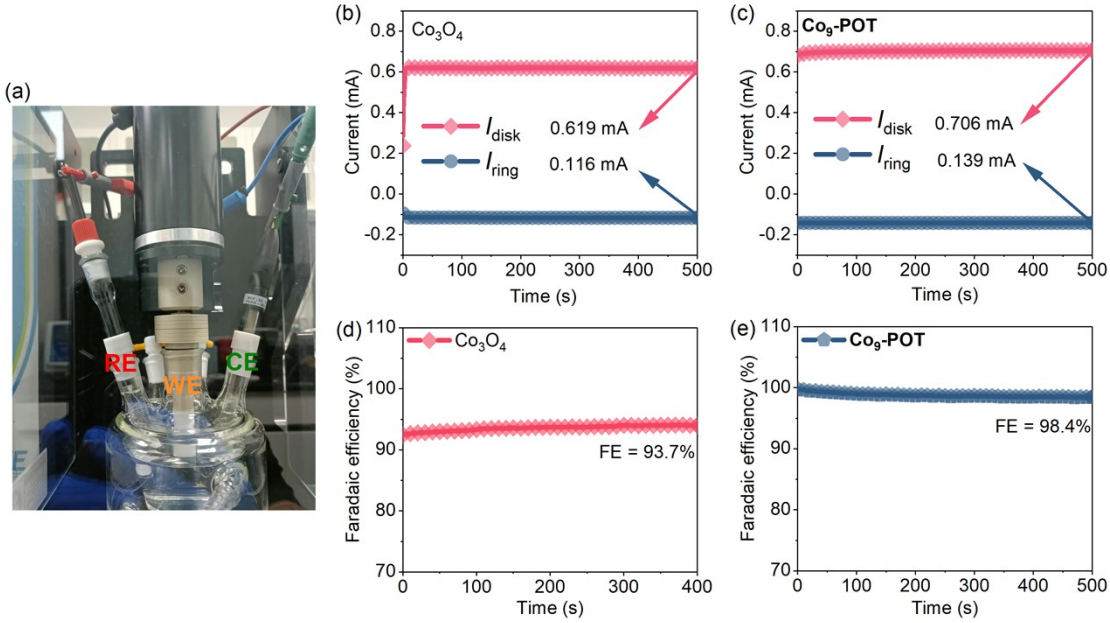

Fig. S15. Faraday efficiency of Co_3O_4 and **Co_9-POT**. (a) Rotating annular disk electrode (PINE) being tested for FE. The disk and ring currents of Co_3O_4 (b) and **Co_9-POT** (d) were tested by the RRDE method; Faradaic efficiency of Co_3O_4 (c) and **Co_9-POT** (e).

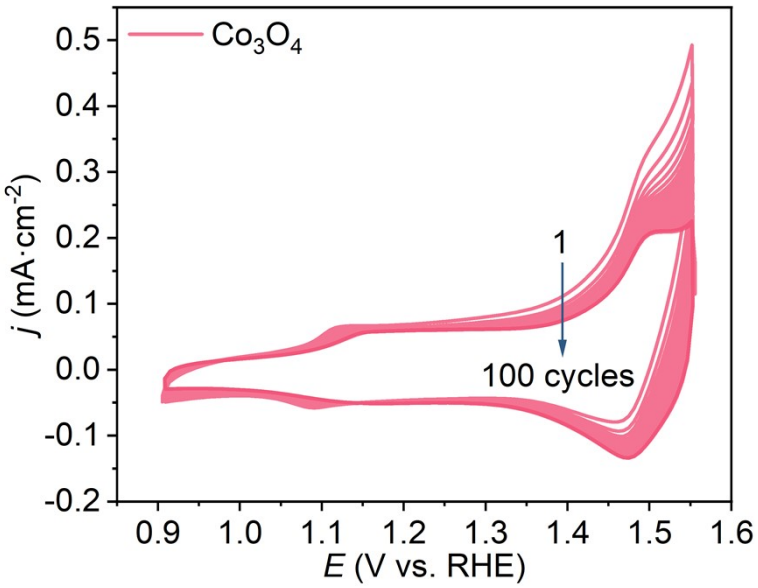

Fig. S16 The CV curves of Co_3O_4 in 0.1 M KOH with a sweep rate of 20 mV s^{-1} and 100 cycles.

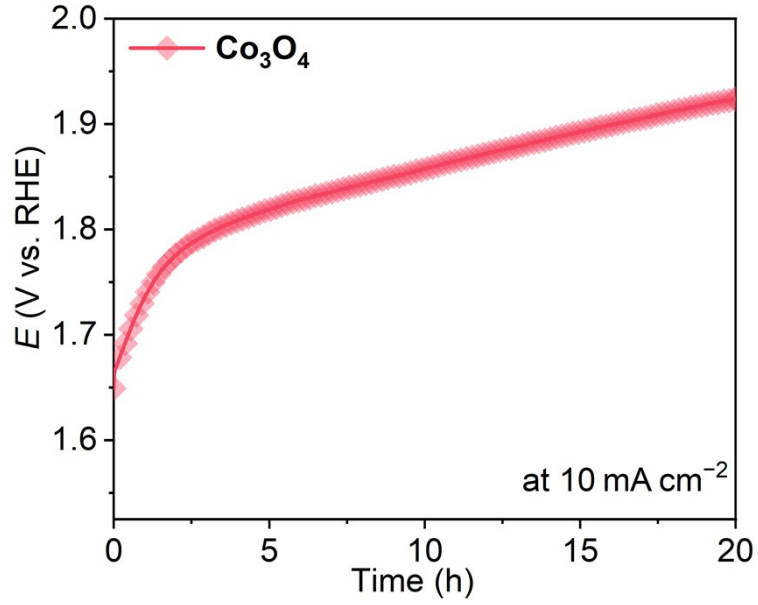

Fig. S17 The chronopotentiometry test of the Co_3O_4 at 10 mA cm^{-2} for 20 h.

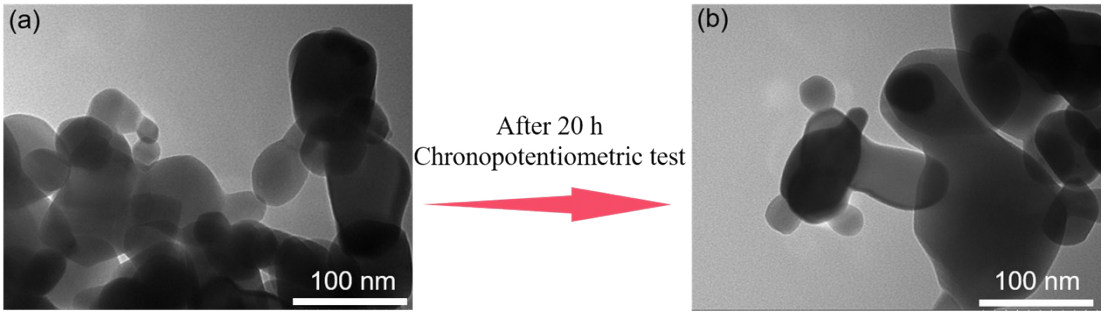

Fig.S18 TEM of Co_3O_4 before and after 20 hours stability test.

A comparative analysis of TEM images of Co_3O_4 before and after the reaction was conducted, and the assay did not reveal the presence of a thick CoO(OH) layer on Co_3O_4 (Fig. S18†). The result suggests that the observed decrease in stability is not primarily due to structural reorganization.

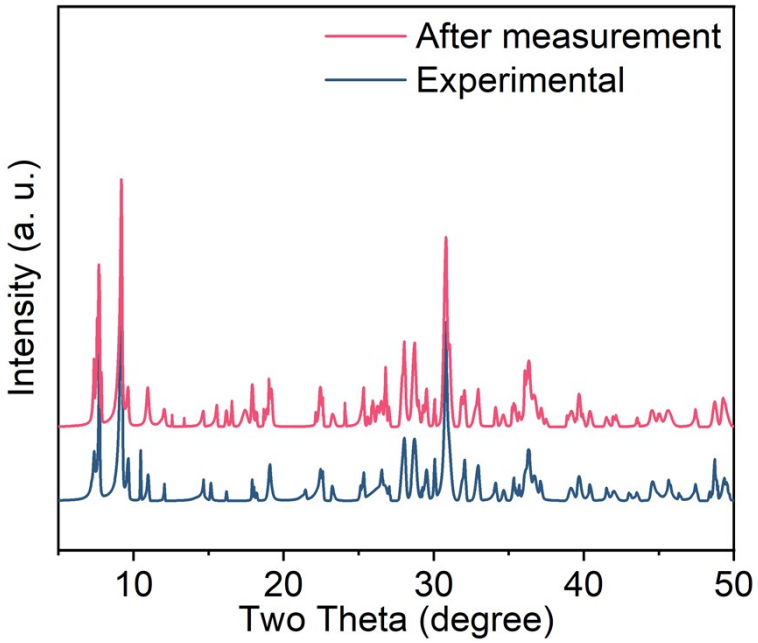

Fig. S19 Powder XRD patterns of **Co_9-POT** before and after 20 hours of OER testing.

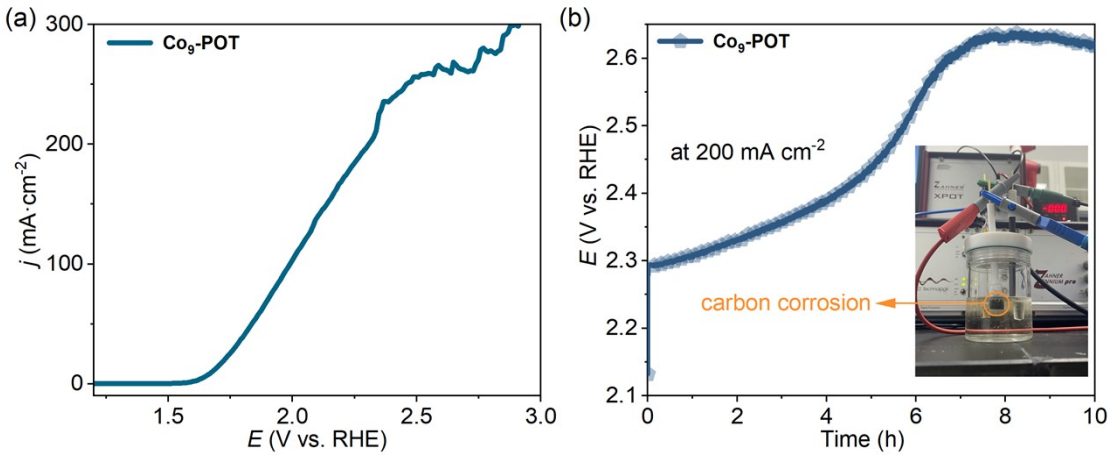

Fig. S20. (a) LSV curve of sample **Co_9-POT** under wide-ranged voltage; (b) Chronopotentiometric curves of **Co_9-POT** toward OER at 200 mA cm^{-2} for 10 h.

As shown in Fig. S20a, the LSV curve was scanned in a wider potential range, and the current became extremely unstable near 2.5 V. This phenomenon may be attributed to the corrosion of the carbon cloth caused by the high potential. A stability curve was scanned at a current density of 200 mA cm^{-2} (Fig. S20b). The results show that the catalyst has been mostly detached, which is the primary cause of the performance decline at high potentials. The performance continues to decline, while the carbon cloth in the electrolyte corrodes gradually and the solution turns slightly yellow.

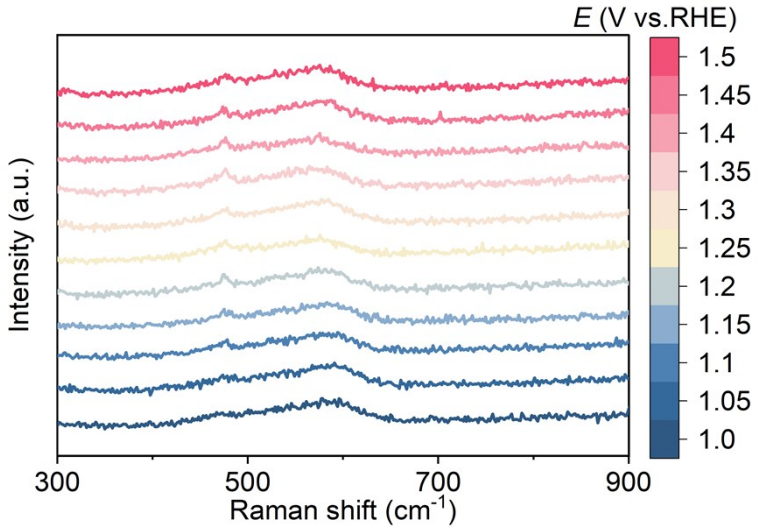

Fig. S21 In situ Raman spectra of **Co_9-POT** at increasing applied potential from 1.1 V to 1.5 V (0.05 V per step) in 0.1 M KOH.

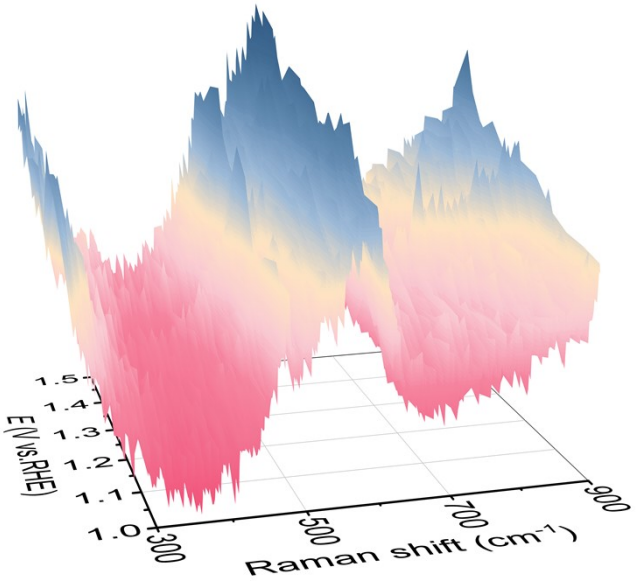

Fig. S22 Three-dimensional spectra of sample **Co_9-POT** in situ Raman.

references

1. Li-Hua Bi, Ulrich Kortz, Saritha Nellutla, Ashley C. Stowe, Johan van Tol, Naresh S. Dalal, Bineta Keita and L. Nadjo, Structure, electrochemistry, and magnetism of the Iron(III)-substituted Keggin Dimer, $[Fe_6(OH)_3(A\text{-}\alpha\text{-}GeW_9O_{34}(OH)_3)_2]^{11-}$, *Inorg. Chem.*, 2005, **44**, 896-903.
2. G. M. Sheldrick, A short history of SHELX, *Acta Crystallogr., Sect. A: Found. Crystallogr.*, 2007, **64**, 112-122.
3. G. M. Sheldrick, Crystal structure refinement with SHELXL, *Acta Crystallogr., Sect. C: Struct. Chem.*, 2015, **71**, 3-8.
4. A. L. Spek, PLATONSQUEEZE: a tool for the calculation of the disordered solvent contribution to the calculated structure factors, *Acta Crystallogr., Sect. C: Struct. Chem.*, 2015, **71**, 9-18.
5. X. Lei, C. Jiang, Q. Han, X.-Z. Fu, J. Li and Y. Sun, Unraveling the oxygen vacancy site mechanism of a self-assembly hybrid catalyst for efficient alkaline water oxidation, *ACS Catal.*, 2024, **14**, 4523-4535.
6. S. Zhao, C. Tan, C.-T. He, J. Dong and Z. Tang, Structural transformation of highly active metal-organic framework electrocatalysts during the oxygen evolution reaction, *Nat. Energy*, 2020, **5**, 881-890.
7. J. Suntivich, K. J. May, H. A. Gasteiger, J. B. Goodenough and Y. Shao-Horn, A perovskite oxide optimized for oxygen evolution catalysis from molecular orbital principles, *Science*, 2011, **334**, 1383-1385.
8. S. Zhao, Y. Wang, J. Dong, S. Liu, H. Zhao and Z. Tang, Ultrathin metal-organic framework nanosheets for electrocatalytic oxygen evolution, *Nat. Energy*, 2016, **1**, 16184.
9. V. K. Abdelkader-Fernández, D. M. Fernandes, L. Cunha-Silva, A. J. S. Fernandes and C. Freire, Decorating MOF-74-derived nanocarbons with a sandwich-type polyoxometalate to enhance their OER activity: Exploring the underestimated bulk-deposition approach, *Electrochim. Acta*, 2021, **389**.
10. V. K. Abdelkader-Fernández, D. M. Fernandes, S. S. Balula, L. Cunha-Silva and C. Freire, Advanced framework-modified POM@ZIF-67 nanocomposites as enhanced oxygen evolution reaction electrocatalysts, *J. Mater. Chem. A*, 2020, **8**, 13509-13521.
11. A. Joshi, P. Sood, A. Gaur, D. Rani, V. Madaan and M. Singh, Improved OER performance of an Anderson-supported cobalt coordination polymer by assembling with acetylene black, *J. Mater. Chem. A*, 2022, **10**, 12805-12810.
12. H. Liu, L.-G. Gong, C.-X. Wang, C.-M. Wang, K. Yu and B.-B. Zhou, $\{Cu_2SiW_{12}O_{40}\}$@HKUST-1 synthesized by a one-step solution method with efficient bifunctional activity for supercapacitors and the oxygen evolution reaction, *J. Mater. Chem. A*, 2021, **9**, 13161-13169.
13. P. Sood, A. Joshi and M. Singh, A rare polyoxometalate cluster $[NiW_{12}O_{44}]^{14-}$based solid as a pre-catalyst for efficient and long-term oxygen evolution, *Nanoscale Adv.*, 2022, **4**, 5015-5020.
14. N. Hu, J. Du, Y.-Y. Ma, W.-J. Cui, B.-R. Yu, Z.-G. Han and Y.-G. Li, Unravelling the role of polyoxovanadates in electrocatalytic water oxidation reaction: Active species or precursors, *Appl. Surf. Sci.*, 2021, **540**, 148306.
15. J. Song, P. Zhu, W. Ma and Y. Li, PW_6Mo_6/ZIF-67@NF composite with exposed Co nodes as efficient oxygen evolution reaction electrocatalyst, *Int. J. Hydrogen Energy*, 2024, **51**, 327-337.
16. Y. Li, X. R. Chang, X. J. Sang, J. S. Li, Y. H. Luo, Z. M. Zhu and W. S. You, Keggin-type polyoxometalate modified Ag/graphene composite materials for electrocatalytic water oxidation, *Eur. J. Inorg. Chem.*, 2019, **2019**, 3597-3604.
17. T. Ahmed, M. A. Asghar, A. Ali, S. Touseef, A. Hussain and A. Haider, High-nuclearity cobalt(II)-containing polyoxometalate anchored on nickel foam as electrocatalyst for electrochemical water oxidation studies, *J. Alloys Compd.*, 2022, **909**, 164709.
18. Y. Bai, Y. Wu, X. Zhou, Z. Liu, T. Cheng and C. Gao, Promoting nickel oxidation state transitions in single-

layer NiFeB hydroxide nanosheets for efficient oxygen evolution, *Nat. Commun.*, 2022, **13**, 6094.

19. B. Pan, X. Peng, Y. Wang, Y. Zhang, T. S. Teets and M. H. Zeng, Tracking the pyrolysis process of a 3-MeOsalophen-ligand based CO_2 complex for promoted oxygen evolution reaction, *Chem. Sci.*, 2019, **10**, 4560-4566.
20. G. J. Brug, A. L. G. V. D. Eedeen, M. Sluyters-Rehbach and J. H. Sluyters, The analysis of electrode impedances complicated by the presence of a constant phase element, *J. Electroanal. Chem.*, 1984, **176**, 275-295.
21. R. L. Doyle and M. E. Lyons, An electrochemical impedance study of the oxygen evolution reaction at hydrous iron oxide in base, *Phys. Chem. Chem. Phys.*, 2013, **15**, 5224-5237.
22. Z.-W. Wang and G.-Y. Yang, A $\{Co_9\}$-added polyoxometalate for efficient visible-light-driven hydrogen evolution, *Molecules*, 2023, **28**, 664.
23. Z. Li, L. D. Lin, H. Yu, X. X. Li and S. T. Zheng, All-inorganic ionic porous material based on giant spherical polyoxometalates containing core-shell $K_6@K_{36}$-water cage, *Angew. Chem. Int. Ed.*, 2018, **57**, 15777-15781.
24. Y.-J. Wang, L. Yu, X.-X. Li, Y.-Q. Sun and S.-T. Zheng, Two unprecedented germanoniobate frameworks based on high-nuclearity peanut-shaped $\{Ge_{12}Nb_{38}\}$ clusters, *Inorg. Chem.*, 2024, **63**, 1388-1394.
25. Z.-Y. Yu, Y. Duan, Y. Kong, J. Zhu, M.-R. Gao and S.-H. Yu, General synthesis of tube-like nanostructured perovskite oxides with tunable transition metal–oxygen covalency for efficient water electrooxidation in neutral media, *J. Am. Chem. Soc.*, 2022, **144**, 13163-13173.